ResearchGate

See discussions, stats, and author profiles for this publication at: https://www.researchgate.net/publication/343039766

Assessment of Compressive Strength of Ultra-high Performance Concrete using Deep Machine Learning Techniques

Article *in* Applied Soft Computing · July 2020

DOI: 10.1016/j.asoc.2020.106552

CITATIONS
21

READS
283

3 authors, including:

Omar R. Abuodeh
Clemson University
12 PUBLICATIONS **84** CITATIONS
SEE PROFILE

Jamal A Abdalla
American University of Sharjah
160 PUBLICATIONS **2,432** CITATIONS
SEE PROFILE

Some of the authors of this publication are also working on these related projects:

Flexural Behavior of Reinforced Concrete Beams Strengthened with Externally Bonded Hybrid Systems View project

Shear strengthening of RC beams using CFRP laminates and anchors View project

All content following this page was uploaded by Omar R. Abuodeh on 18 July 2020.

The user has requested enhancement of the downloaded file.

Assessment of Compressive Strength of Ultra-high Performance Concrete using Deep Machine Learning Techniques

Omar R. Abuodeh[1,*], Jamal A. Abdalla[2] and Rami A. Hawileh[3]

[1] Graduate Student, Glenn Department of Civil Engineering, Clemson University, Clemson, SC, 29634, USA, Email: oabuode@g.clemson.edu
[2] Professor, Department of Civil Engineering, American University of Sharjah, UAE, Email: jabdalla@aus.edu
[3] Professor, Department of Civil Engineering, American University of Sharjah, UAE, Email: rhaweeleh@aus.edu
[*] Corresponding Author.

Abstract

The compressive strength of Ultra-High Performance Concrete (UHPC) is a function of the type, property and quantities of its material constituents. Empirically capturing this relationship often requires the utilization of intelligent algorithms, such as the Artificial Neural Network (ANN), to derive a predictive model that fits into an experimental dataset. However, its black-box nature prevents researchers from mathematically describing its contents. This paper attempts to address this ambiguity by employing two deep machine learning techniques—Sequential Feature Selection (SFS) and Neural Interpretation Diagram (NID)—to identify the critical material constituents that affect the ANN. 110 UHPC compressive strength tests varying based on the material quantities were compiled into a database to train the ANN. As a result, four material constituents were selected; mainly, cement, fly ash, silica fume and water. These material constituents were then employed into the ANN to compute more accurate predictions (r^2 = 80.1% and NMSE = 0.012) than the model with all eight material constituents (r^2 = 21.5% and NMSE = 0.035). Finally, a nonlinear regression model based on the four selected material constituents was developed and a parametric study was conducted. It was concluded that the utilization of ANN with SFS and NID drastically improved the accuracy of the model, and provided valuable insights on the ANN compressive strength predictions for different UHPC mixes.

Keywords: Compressive Strength; Ultra-High Performance Concrete; Deep Machine Learning; Sequential Feature selection; Neural Interpretation Diagrams.

Nomenclature

X	Input parameters in the form of a matrix
θ^k	A matrix composed of randomly generated weights per layer k
$O(X)$	Vector form of predictions
$g(x)$	Activation function
b^k	Vector composed of the bias units in layer k
J	Jacobian matrix $\frac{\partial f(P)}{\partial P}$
ε	Error or *cost*
δ_P	Solution when $\mathbf{J}\delta_P$ is orthogonal to the column space **J**

i	Individual number of neurons
n	Total number of neurons
a	Hidden neuron
SSR	Sum of squared residuals
Cov	Covariance matrix
f_c	Concrete compressive strength
A/B	Regression coefficients

1. Introduction:

Machine learning algorithms such as Artificial Neural Network (ANN) have been extensively used, in different fields, to evaluate predictive outcomes that closely agree with the experiment. However, an experiment could consist of a comprehensive test matrix with a large number of parameters in which the majority exhibits little contribution to the test outcomes. This necessitated computer scientists to develop novel selection algorithms based on data-driven models; thereby identifying the most relevant independent variables and rapidly reducing the dimensionality of the input matrix. The need for soft computing tools in predictive modeling of engineering components, systems and materials is continuously rising; where ANN emerged as one of the most popular soft computing paradigms that have been successfully applied in several engineering fields [1]. Generally, ANN has been implemented in the prediction and approximation of character and pattern recognition, image processing, forecasting, classification, optimization, and control related problems [1]. This advocated researchers to propose ANN models and solve a wide variety of civil engineering problems [2–7]. Furthermore, extensive applications in ANN behavioral modeling of concrete structural elements have been reported in several studies [8–15]. In recent years, research interests have migrated towards utilizing different ANN models to solve predictive-based challenges of building material like: steel, concrete, and composites [16–20]. The majority of problems related to concrete characteristics like fresh and hardened properties have been successfully addressed using ANN modeling based on collected experimental data. Moreover, prediction of concrete compressive strength using ANN models has been an area of continuous research in the recent years. This, in turn, motivated researchers to employ ANN computing for evaluating compressive strength of normal weight, light weight and recycled concrete [21–25]. Other researchers investigated various predictive models to interpret the compressive strength of high performance concrete using different machine learning techniques [26–28]. Afterwards, the emergence of ultra-high performance concrete (UHPC) necessitated further development of ANN modeling towards behavioral predictions.

Researchers have successfully developed ANN models to accurately simulate the performance of UHPC [29–31], however, these black-box paradigms offer little insights on what takes place during ANN computations. Therefore, addressing this ambiguity should be the next step in advancing the movement of implementing intelligent algorithms when assessing the performance of UHPC mixes, while mathematically demonstrating it. Application in deep machine learning have shown promising works in this regard where the optimization techniques that take place during an ANN training phase is leveraged to iteratively select the parameters that influence the

model's accuracy [29–31]. The selected parameters can then be employed into the ANN, or any other intelligent regression algorithm, to improve the accuracy of the predictive model while understanding the physical phenomenon behind these selections.

In this investigation, a deep machine learning technique based on an ANN, which employs deep machine learning algorithms in identifying the critical parameters that influence the accuracy of predicting the compressive strength of UHPC, is presented. A comprehensive database of experimental results, with several parameters, is collected from published UHPC compressive strength tests. Afterwards, a series of ANNs pertaining different architectures were iteratively employed to consistently obtain a final model. This model is then used with SFS and NID to systematically select the material constituents that influence the model's predictions of UHPC compressive strength. Finally, the previously selected material constituents are used to derive an analytical model and perform parametric studies to investigate their relationships with the compressive strength of UHPC.

2. UHPC and ANN: Background

The evolution of UHPC has led structural engineers to improve the compressive strength, ductility, and durability of heavy loaded reinforced concrete structures. Several researchers have investigated the mechanical behavior of UHPC and its applications over the last four decades [32], where UHPC usually exhibits a compressive strength that would range from 150 MPa to 810 MPa [33–35]. The ingredients required to produce such high compressive strength material are: (a) high dosage of cement (up to 800 kg/m^3); (b) lower water/binder ratio (lower than 0.20); (c) high-range water-reducing (HRWR) admixture; (d) very fine powders (crushed quartzite, silica fume, and nano-silica); and (d) steel fibers and/or polyethylene fibers [36, 37]. Other researchers aimed at developing sustainable and economical approaches by reducing the amount of cement and silica fume, and compensate these reductions with the addition of fly ash and sand [38–40]. However, most of the aforementioned mixtures result in exhausting a large amount of resources and performing tests on many batches, while barely predicting the strength of UHPC [41]. Therefore, acquiring an analytical model that is a function of the constituents of UHPC is needed to easily and accurately predict compressive strength values [29–31].

Ghafari et al. [29] investigated the implementation of back-propagation neural network (BPNN) and statistical mixture design in predicting the required performance of UHPC. Their objective was to predict both the compressive strength and the consistency of UHPC with two different types of curing, mainly, steam curing and wet curing, using both BPNN and statistical mixture design. Fifty three concrete specimens were designed based on the design matrix of the statistical mixture design, and the constituents that make up the mixture were taken as the independent parameters of the BPNN model. The results indicated that BPNN was capable of predicting the compressive strength and slump flow with higher accuracy than the statistical mixture design. Kasperkiewicz et al. [30] used ANN to predict the optimal mix proportion of cement, silica, superplasticizer, water, fine aggregate, and coarse aggregate of high performance concrete (HPC), despite having data complexity, incompleteness, and incoherence. Their model showed a significant correlation between the actual and the predicted values observed, where an optimum mix can be approximated using an ANN model. Awodiji et al. [31] trained a series ANN models to investigate the relationship between the compressive strength and ratio of material quantities to curing age for different hydrated lime cement concrete mixes. As a result, the models

achieved correlation coefficients that ranged between 90.1–98.4%; indicating that the models were successful in predicting the compressive strength for different concrete mixes. Although the accuracy of the previously proposed ANN models [29–31] were reasonable, nevertheless, the reduction of input parameters will simplify the ANNs architectures and enhance their models' computational efficiency. Therefore, researchers developed robust techniques that can reveal the contents within the ANN model by means of identifying the most influential independent parameters that can be used to improve the accuracy of the ANN.

3. Related Works

Feature selection is an example of one of the developed techniques in which the algorithm identifies the features contributing strongly to the prediction model by sorting the feature subsets based on a user-imposed evaluation measure (i.e., error/performance), which scores differently for every added feature subset. This intelligent selection process improves the performance of the model, in terms of accuracy and precision, and facilitates a better understanding of data processing [42, 43]. There are two types of feature selection classes; mainly *filter method*, which highlights the intrinsic characteristics of the independent variables measured by means of fundamental statistics, and *wrapper method*, which measures the efficiency of the independent variables based on the regression/classification model's performance [44–46]. This study focused primarily on incorporating the wrapper method, Sequential Feature Selection (SFS) algorithm.

Zhou et al. [45] used the SFS paradigm within the Markov Blanket, another machine learning technique, to select the most critical features of human motion recognition. As a result, the total number of features was rapidly reduced where this improved the algorithm's capabilities of showing better recognition accuracy than traditional methods. Rodriguez-Galiano et al. [46] also used SFS when tackling ground water quality problems where 20 parameters were extracted from a comprehensive database. This study implemented four types of machine learning algorithms with SFS, and located the underlying parameters impacting the performance of each machine learning technique. As a result, the Rain Forest machine learning algorithm used with SFS showed promising results, where only three features were necessary to predict the most accurate results. Besides SFS learning tool, another variable importance method, termed neural interpretation diagram (NID), was employed by Ozesmi et al. [47] to study the spatial models for habitat selection of marsh-breeding bird species. This algorithm was incorporated within an ANN model to visually inspect the bearing-effect of each habitat variable, with respect to the classification approach, and successfully obtain the critical parameters from the total dataset. Afterwards, the authors employed these candidate parameters into a new ANN model; thereby providing them a better understanding of the mechanisms of habitat selection.

This study aims at utilizing SFS and NID within a BPNN to successfully identify the material constituents that contribute to the compressive strength of UHPC. The machine learning tools analyzed eight material constituents from 110 UHPC compressive strength tests, collected from a comprehensive database [48–59], and selected the dominant and most influential features that enhance the performance of the BPNN model. In addition, Abram's classical model for predicting concrete compressive strength was modified using the selected features and the regression coefficients were derived based on a minimization algorithm through the nonlinear regression analysis. Finally, a parametric study was conducted, using the selected features, to investigate the behavioral impact of each material constituent on the compressive strength of UHPC.

4. Methodology of modeling:

The investigation conducted was based on four systematic steps; mainly, data collection, verification of BPNN, execution of SFS and NID, and analysis of selected features. **Fig. 1** outlines this approach within a flowchart where it was possible to develop a robust and accurate predictive model. The first and second boxes (Input Data and Design/Validate BPNN Model) elucidate the process of iteratively training the data until a BPNN structure that can make both accurate and consistent predictions is obtained. The third box (Execute SFS/NID) highlights the employment of deep machine learning algorithms (SFS and NID) to systematically select the material constituents that influence the accuracy of the BPNN predictions during the training phase. The last box (Analyze Selected Material Constituents) consists of carrying out a comprehensive parametric study that underscores the relationship between the compressive strength and the variations in material quantities in different UHPC mixes.

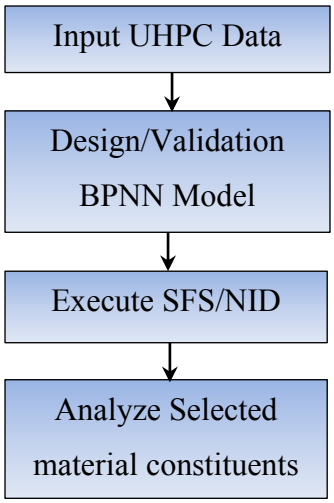

Fig. 1. Flowchart of the Deep Machine Learning Approach

Table 1 presents the common constituent materials of UHPC mixes used in different experimental investigations [49–59] with their corresponding code names and statistical measurements; the maximum, minimum, mean, median, and standard deviation. A detailed list of the parameters tested during this study can be found in Appendix A (Table A.1). In addition, all compressive strength values were measured after 28 days from casting. A nested plot composed of the frequency distributions for each material constituent investigated in this study is presented in **Fig. 2**.

Table 1: Range of input parameters for training, validation and testing

Symbol		Statistical Measurements				
Variable	Coded	Minimum	Maximum	Mean	Median	Standard Deviation
Cement (kg/m^3)	C	383	1600	879.7	786	329.8
Silicafume (kg/m^3)	SI	0	367.95	192.0	196	94.6

Flyash (kg/m^3)	FA	0	448	33.0	0	72.7
Sand (kg/m^3)	SA	0	1898	980.0	1107	513.8
SteelFiber (kg/m^3)	SF	0	470	39.0	0	74.8
QuartzPowder (kg/m^3)	QP	0	750	36.9	0	125.9
Water (kg/m^3)	W	109	334.5	197.1	185.3	54.3
Admixture (kg/m^3)	A	0	185	31.9	30.1	28.2
f'c (MPa)	fc	95	240	152.2	147.9	31.5

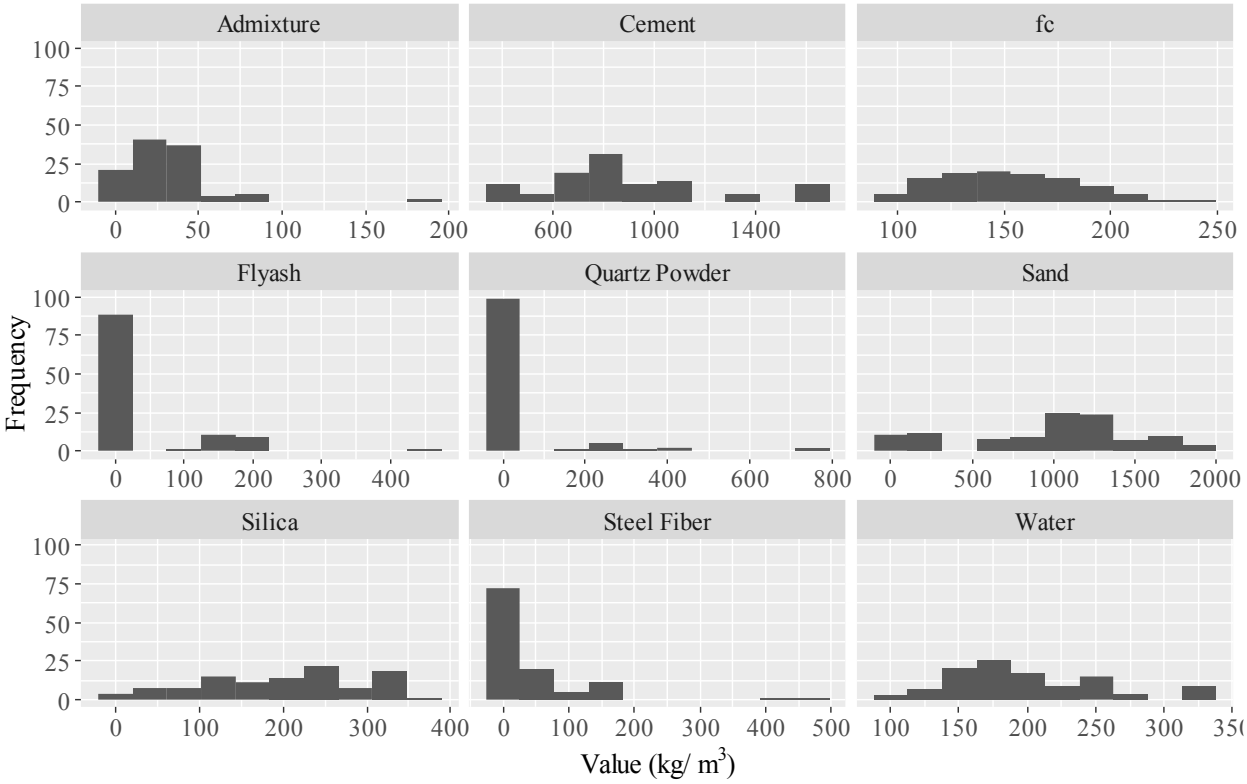

Fig. 2. Frequency Distribution of Experimental Data

4.1.Artificial neural network:

ANN is a machine learning paradigm that mathematically imitates the learning functions of a human brain in the sense of analyzing different experiences registered by the neurons and locating an accurate solution based on a trial-and-error approach. There are two types of ANN models: (1) feed forward; and (2) feed backward. The feed forward requires that the ANN model to have an adjusted or *learned* network, by means of a back-propagating (BP) technique in order to make predictions. The feed backward model attempts to approximate the predictor variables and uses the true response variables to compute the cost or *error* between them. Afterwards, the algorithm adjusts the weights such that the network converges on the most accurate solution. For this reason, the BP feed-forward multilayer perceptron was extensively used in different engineering applications [12, 22, 29].

The architecture of a typical ANN is composed of input neurons, hidden neurons, bias units, wires, and output neurons. The input neurons consist of each parameter in the form of a vector

(input by the user), the wires represent randomly generated matrices called weights that manipulate the function's slope or steepness, the hidden neurons map the weights variables using user-defined activation functions, and the bias units control the output function's shift; either upward or downward.

Eq. (1) shows a vertorized form of the complex combinations during the analysis period for a single-hidden layered system.

$$O(X) = g(\theta^k X + b^k) \quad (1)$$

Where X represents the input parameters in the form of a matrix, θ^k is a matrix composed of randomly generated weights per layer k (starting from the hidden layer), $O(X)$ is the vector form of predictions, g(x) is the activation function and b^k is a vector composed of the bias units in layer k.

Prior to the final output, each row was transformed within a certain domain using a user-defined activation function. In this study, the sigmoid function was used as presented in eq. (2).

$$g(x) = \frac{1}{1 + e^{-O_i}} \quad (2)$$

The BP technique uses a minimization cost approach, Levenberg-Marquardt algorithm, which is an iterative technique that locates the *local* minimum of a multivariate function expressed as the sum of squares of non-linear real-valued functions. The Levenberg-Marquardt algorithm uses both the Gradient Descent Method and Gauss-Newton method to help the solution converge [60]. Eq. (3) summarizes the iterative technique in an algebraic matrix form.

$$\mathbf{J}^T\mathbf{J}\delta_P = \mathbf{J}^T\boldsymbol{\varepsilon} \quad (3)$$

Where $\mathbf{J}$ is the Jacobian matrix $\frac{\partial f(P)}{\partial P}$, ε is the error or *cost* $\left(J(\theta) = \left\|\frac{1}{2R}\sum_{r=1}^{R}(O(X^r) - Y^r)^2\right\|\right)$, and δ_P is the solution when $\mathbf{J}\delta_P$ is orthogonal to the column space $\mathbf{J}$. By altering or *damping* the elements in $\mathbf{J}^T\mathbf{J}$, the cost ε varies and δ_P is calculated. Afterwards, θ is adjusted using eq. (4) and $O(X)$ is recalculated using eq. (1). This algorithm reiterates until ε decreases leading to a reduction in the damping rate as the solution slowly converges.

$$\theta_1 = \theta_0 + \delta_P \quad (4)$$

Where θ_1 and θ_0 represent the adjusted weights and initial weights, respectively.

Fig. 3 displays the schematics of an ANN with one input layer, one hidden layer, and an output layer. Both the subscripts and superscripts are used to identify the neuron and layer numbers, respectively. Ultimately, the subscripts i and n are used to identify the individual and total number of neurons, respectively, within the input layer k. Each input neuron, X_i, contains one independent parameter and X_{i+1} contains the subsequent column until n neurons are passed into the BPNN structure. Similarly, the subscripts j and m also denote the individual and total number of neurons, respectively, within an arbitrary hidden layer $k+1$, where each hidden neuron, a_j^{k+1}, receives weighted matrix-products from each neuron, X_i, via the wires connecting between the input and hidden layers. These wires contain weights, θ, and are responsible for transforming the mapped sum-products into the neighboring layers.

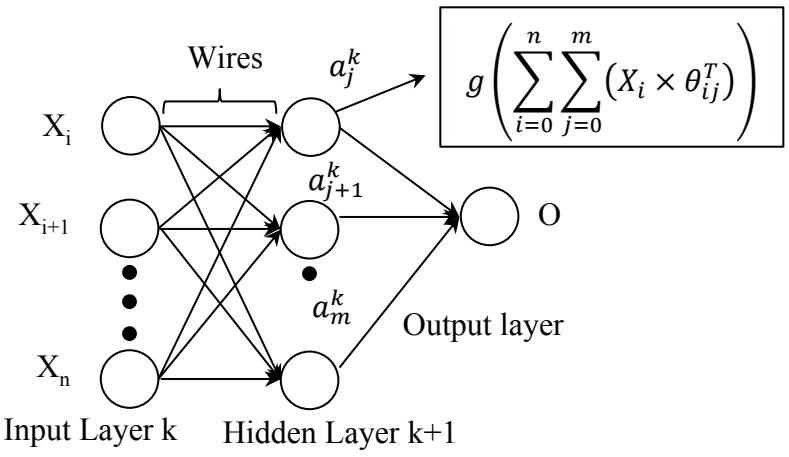

Fig. 3. ANN Architecture

4.2.Sequential Feature Selection:

Feature selection reduces the dimensionality of data by selecting a subset of measured features and to build a simpler prediction model [61]. This machine learning algorithm is composed of two components: the objective function, which is the criteria the algorithm tracks when selecting the features, and the search algorithm, which is the approach the machine learning tool uses to add/remove features from a subset. A popular search algorithm used in several studies [44–46] is the Sequential Feature Selection (SFS), which is a function that is initialized during a predictive model assessment and it sequentially appends variables into the model until any further addition does not yield a sufficient change in the objective function. In this study, the objective function used was the Normalized Mean Square Error (NMSE), and the search algorithm implemented was SFS within a BPNN. **Fig. 4** shows the algorithm SFS uses when performing a selection.

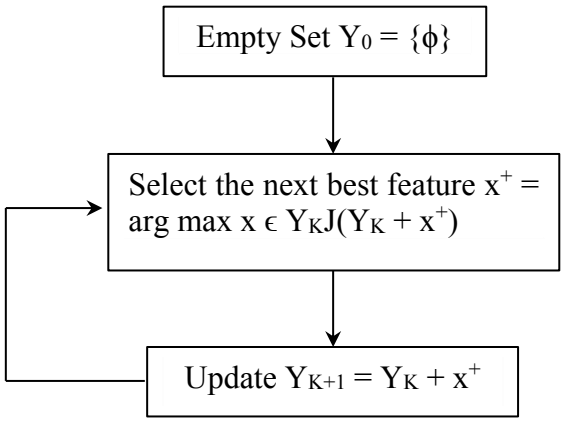

Fig. 4. Forward Selection Algorithm

4.3.Neural Interpretation Diagram

Neural interpretation diagram (NID) is an ANN structure that demonstrates the relative importance an independent variable has with the response variable in terms of the weights' magnitudes and signs. The algorithm deconstructs the weights for each input node during the analysis stage until a list of all weights is stored in a matrix. Afterwards, the matrix is equated to each input node and scaled relative to all the other input variables, and a single value is obtained for each input variable that describes the relationship with the response variable in the model. This information helps users identify the type of correlation the network facilitates and notifies them which input variables are irrelevant and suppressed by the weights. The opposite is observed for the network whose input parameters have positive associations with the network, i.e., more relevant. **Fig. 5** shows an example of an NID diagram with one hidden layer and one output unit. The solid blue lines represent the positive affiliation from one neuron to the neighboring neuron(s), where the thicker lines indicate stronger associations, whereas a red line indicates negative association of the input variable with the network and hindering the accuracy of the prediction model.

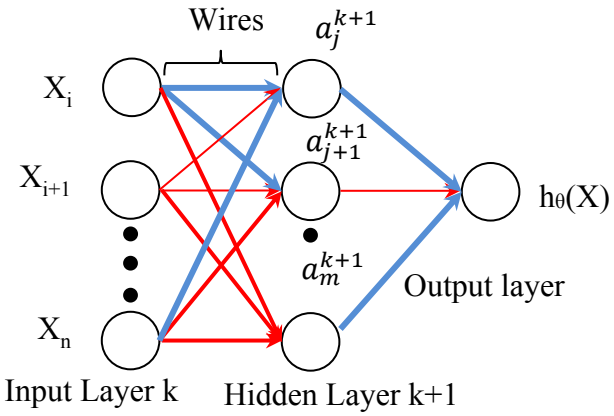

Fig. 5. NID Diagram

4.4.Nonlinear Regression:

One of the objectives of this study is to produce an analytical model with the selected features from the aforementioned methods, SFS and NID. The nonlinear regression is used when the dependent and independent variables are not simultaneously linear. It estimates an arbitrary nonlinear function such that the cost or *standard error* between the theoretical and experimental results is minimized. These estimations are carried out by iteratively selecting appropriate parameters according to the standard error; where the parameters can be multiplicative coefficients and/or exponents. The standard error is a function of the parameters and is shown in eq. (5), where *SSR* is the sum of the squared residuals, *n* is the number of data points in the dataset, and *Cov*(*i*,*i*) is the *i*-th diagonal element in the covariance matrix.

$$S_{Error}(P_i) = \sqrt{\left(\frac{\sum SSR}{n-1}\right) \times Cov(i,i)} \tag{5}$$

The parameters are initialized by the user in which poor assumptions can lead the model to diverge from the actual result; therefore, implementing SFS and NID will reduce the independent parameters and improve convergence during the analysis. Since Abram's formula [62] is applicable for predicting the compressive strength of 7-days and 28-days old concrete, it was used as a mathematical structure during the nonlinear regression analysis, as shown in eq (6). Nonlinear regression was carried out using IBM SPSS 23 software package.

$$f_c = A \times X^{-B} \tag{6}$$

Where X is the water-to-binder ratio, and A and B are regression coefficients.

5. ANN Modeling for prediction of compressive strength of UHPC

5.1.Design of ANN

In this study, BPNN was used to make predictions and to identify the most relevant features. The BPNN was constructed in MATLAB [61] using the Levenberg-Marquardt minimization algorithm. The training parameters like the total epoch, learning rate, and minimum gradient were 1000 epochs, 0.001, and 10^{-7}. A total of 110 observations with eight material constituents were used to train and test the BPNN model, where the UHPC constituents were normalized and written as a ratio of the material constituent to cement. This helped avoid heavy fluctuations in the results and minimized any extreme outliers in the dataset. Table 2 shows the normalized parameters range (maximum and minimum) as a percentage of cement, and the compressive strength values (maximum and minimum).

Table 2: Training and Testing Normalized Data

Symbol		Range	
Variable	Symbols	Minimum	Maximum
Cement	C	1	1
Silica fume	SI	0	0.333
Fly ash	FA	0	1.01
Sand	S	0	4.70
Steel Fiber	SF	0	0.448
Quartz Powder	QP	0	0.938
Water	W	0.1084	0.515
Admixture	A	0	0.282
f'c (MPa)	fc	95	240

5.2.Verification of ANN

There are two types of verification strategies to be employed within the BPNN; mainly, the numerical solver verification and the over fitting verification. The numerical solver verification is the process in which the number of neurons is iteratively increased with each BP analysis. During each run, the error is stored in a vector and plotted versus the corresponding number of neurons. The over-fitting verification is used to ensure that the BPNN does not memorize how to interpret a specific range of inputs such that it can be implemented to predict results using a newly collected

database. For the first type of verification, the BPNN's numerical solver, Levenberg-Marquardt, was verified by testing an arbitrary range of neurons and measuring the performance of the model per neuron using NMSE as indicator. In this study, the increment started from one neuron and ended with 15 neurons, where the model was analyzed 10 times for each neuron. Therefore, for each neuron trained, ten NMSE values were evaluated and stored in a matrix while the mean and 95% confidence interval were calculated for each column vector (neuron) and represented as a dashed line and a shaded region, respectively, versus the number of neuron(s). **Fig. 6** shows the plot of all the trained analyses with the minimum average NMSE point circled at 11 neurons, and the upper and lower confidence interval shown in the light blue shaded area. While implementing the first verification process, the second verification process was implemented in which the data was randomly split into three sets; 70% for the training set, 15% for the validation set, and 15% for the testing set. By combining both processes, the verification strategies resembled that of a k-fold cross-validation approach where the model's input parameters were randomly divided into segregated sets and trained multiple times until the best performing ANN was constructed. **Fig. 7** shows the verified ANN architecture where the neurons inscribed with the letters 'I' and 'H' followed by a number are the input and hidden neurons with their corresponding number of units, respectively, and the neurons with the letters 'B' and 'O' followed by numbers are the bias and output units, respectively. A published article has shown that a double-layered ANN is sufficient enough to simulate the nonlinear behavior of UHPC [36]. Therefore, seven neurons were used in the first hidden layer and three neurons were used in the second hidden layer.

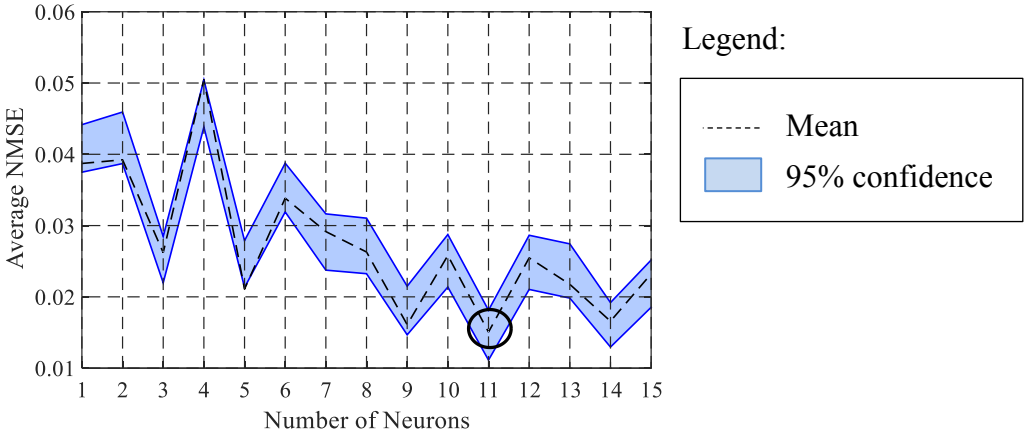

Fig. 6. Verification Plot for ANN

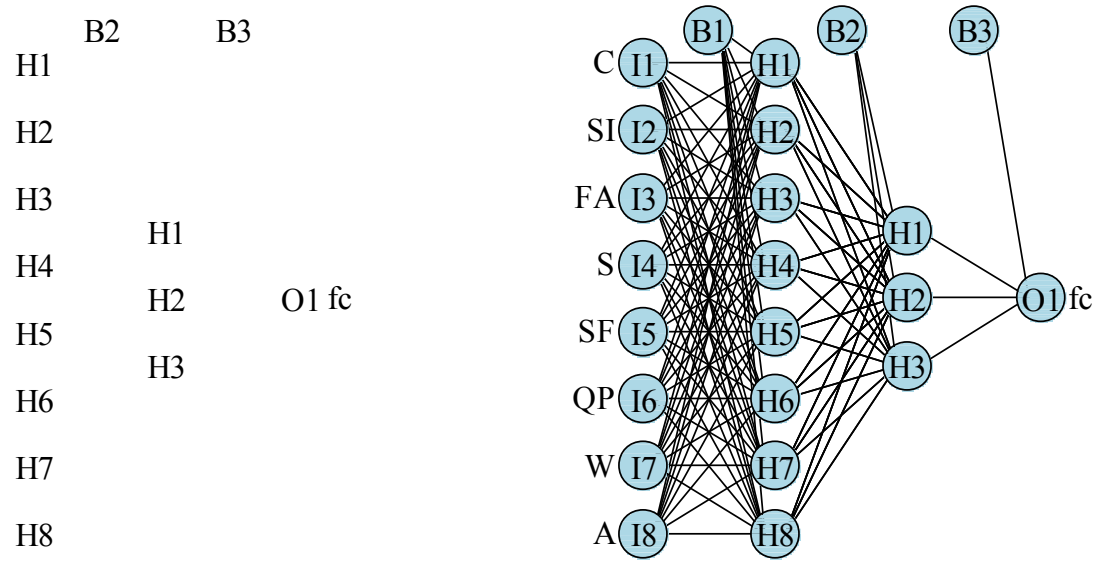

Fig. 7. ANN Architecture

6. Variable importance methods

6.1.Execution of SFS

The SFS algorithm was executed 200 times to capture all possible combinations of independent features when using a BPNN. **Fig. 8** shows a bar plot representing the percentage of features that were used during the 200 trials. Based on the results of these trials and the most dominant combination during the analysis, a threshold of 20% was imposed as the lower bound for selecting the variables that have the largest contribution. The reason for selecting 20% was dependent on the shape of the bar chart, whereby a pattern was shown when observing the small percentage difference between the four variables that have contributed more than 20% of trials. Therefore, the four variables; Cement, Silica Fume, Flyash, and Water were selected as the most relevant features within the prediction model. While preparation techniques and curing regimes have been regarded as significant factors for enhancing the performance of UHPC [32], it has also encouraged on-going investigations in the effect that the material constituents exhibit on the compressive strength of UHPC [38]. Furthermore, researchers have conducted experimental investigations using these exact material constituents to individually monitor the performance of UHPC in terms of compressive strength [57].

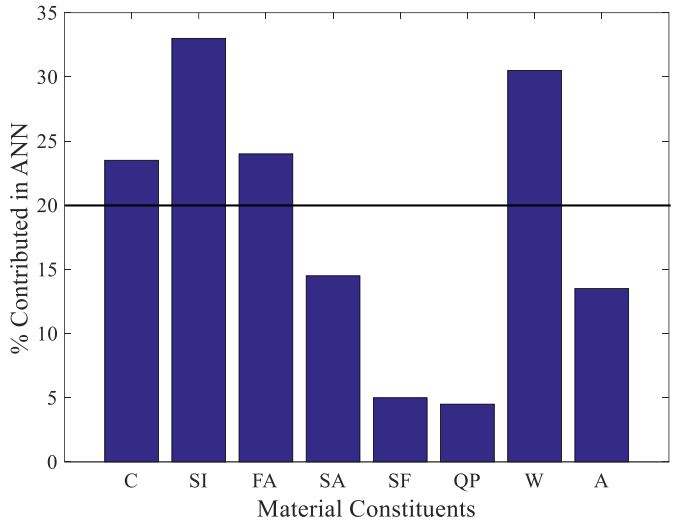

Fig. 8. Bar Plot of the Percentage of Features that Contributed to the Model

6.2.Execution of NID

The NID [47] was used to verify the selected parameters in the SFS method where it was plotted within the verified ANN to visually inspect the features during the analysis. Since the weights dictate the relative influence of information that is processed in the network, a positive association with the response is represented with a solid blue line and a negative association with the response is represented with a red line as previously indicated in **Fig. 5**. The NID was plotted using the statistical programming package, R [47]. **Fig. 9** shows the NID diagram using the previously verified ANN model. It is clearly observed that C, SI, FA, and W demonstrate strong positive association during the analysis, where SI and W show the most dominant positive associations with their neighboring hidden units similar to the bar plot in **Fig. 8**. This was visually measured according to the thickness, color and number of blue wires shown in **Fig. 9** where most of these wires consisted of positive large weighted values that indicate their influential characteristics in the BPNN model. As a result, the selected constituents in this section match with the material constituents selected from the previous section; hence, the utilization of both SFS and NID have shown consistency in identifying features within a predictive model. This proves that the existence of large databases, like the one in this study, enabled the use of advanced machine learning algorithms to successfully identify the influential parameters of the function and thus gave room for the incorporation of statistical toolboxes (i.e., nonlinear regression) to develop a simple robust model for approximating the compressive strength of UHPC without inclusion of other parameters.

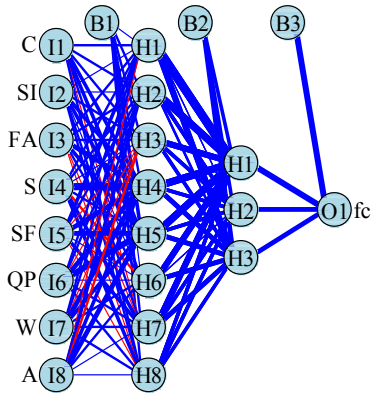

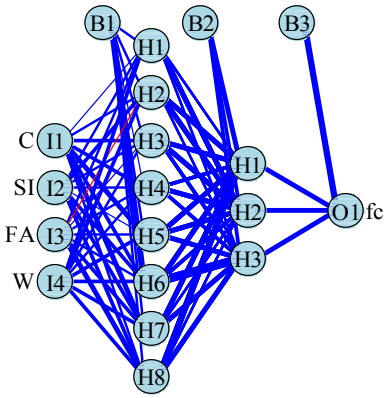

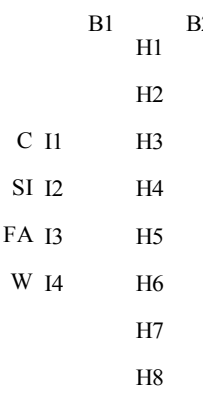

7. Results and discussions

7.1.ANN results

The selected features, i.e., influential parameters, were employed into a new BPNN model to study their performance. As a result, the trained ANN that used the selected features showed stronger agreement with the experimental results in contrast with the ANN prior to the selection. Table 3 shows the statistical measurements calculated for both cases in which the coefficient of multiple determination (r^2) was used to measure the variation between the prediction model's data and its mean compared to that of the experimental results. The NMSE was used to measure the overall variation between the predicted and experimental results. It was observed that the r^2 value before and after selection was 21.5% and 80.1%, respectively, and the NMSE before and after selection was 0.035 and 0.012, respectively.

Table 3: Statistical Measurement using ANN Before and After SFS/NID

Statistics Measurements	Before Selection	After Selection
r^2	0.215	0.801
NMSE	0.035	0.012

Furthermore, correlation plots between the predicted and experimental results were generated for both the trained ANN models, as shown in **Fig. 10**, where the red line represents a perfect fit to the data and the dotted lines represent the percent deviation (±15%) from the perfect fit. As a result, the ANN with the selected features was able to make 80.1% of its predictions within the ±15% threshold whereas the ANN with all the features was able to make 61% of its predictions within the same threshold. This concluded that the model with the selected features outperformed the model with all the features.

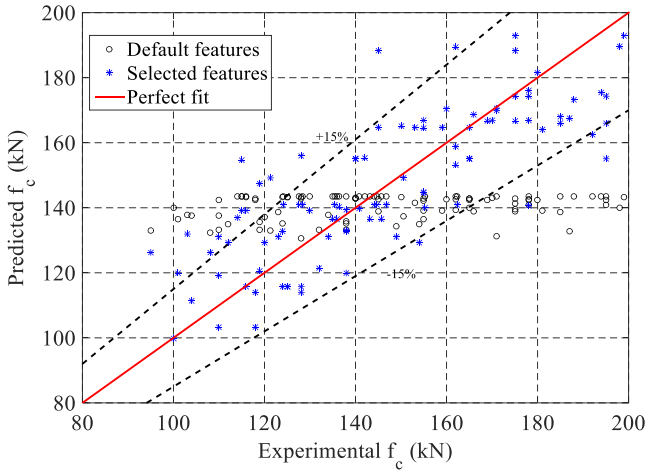

Fig. 10. Percent Deviation of Predicted versus Experimental

Fig. 11 summarizes the predicted-to-experimental compressive strength ratio for both ANN models, where the model with the selected features demonstrated better performance with higher percentage of values (89.1%) ranging between 0.8 and 1.2 than the ANN with all features, (65.4%).

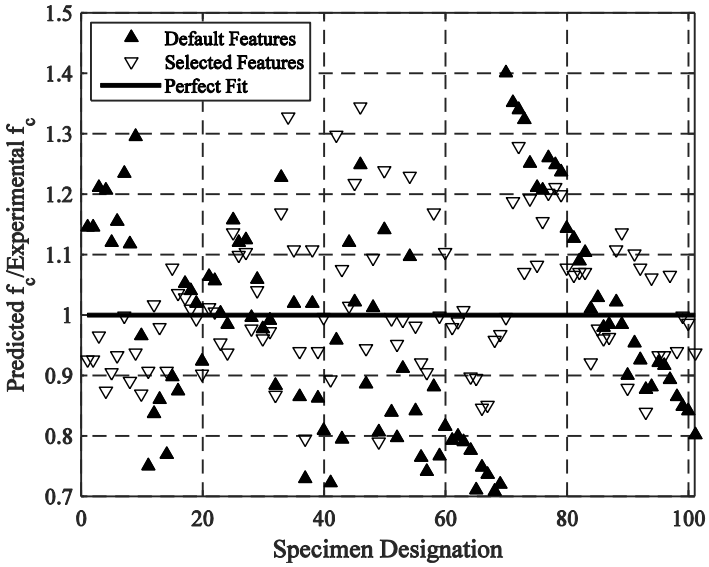

Fig. 11. Ratios of Experimental and Predicted for Both ANN Models

7.2. Developed Model based on Nonlinear Regression Analysis:

Abram's formula, given in eq. (6), was rewritten by explicitly expanding X to a water-to-binder form as given in eq. (7) and initiated within a nonlinear regression analysis using IBM SPSS 23. The material constituents; W, C, SI, and FA were written in kg/m^3. As a result, the regression coefficient values with the statistical measurements are tabulated in Table 4 where the proposed model's r^2 and NSME values were 71.6% and 0.0645, respectively.

$$f_c = A \times \left(\frac{W}{(C + SI + FA)}\right)^{-B} \quad (7)$$

Table 4: LSG Coefficients

Regression Coefficients	Coefficients Values	r^2	NMSE
A	93	0.716	0.0645
B	0.35		

Fig. 12 summarizes the performance of the proposed model and the correlation between the predicted and experimental compressive strength results.

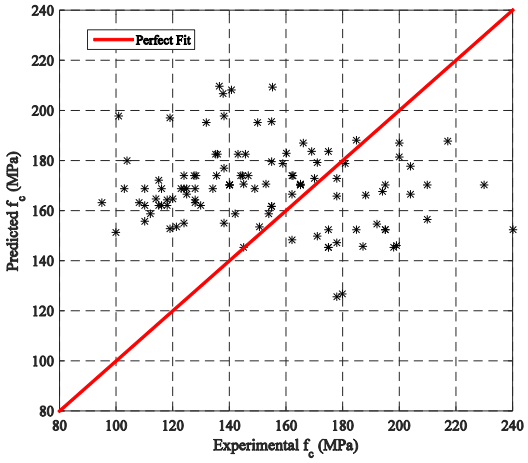

Fig. 12. Summary of the Proposed Model's Performance

Although the ANN model developed in this investigation predicted the concrete strength with high level of accurately, however, the accuracy of the ANN prediction model and its limitation in predicting concrete strength is bounded by the boundaries of the input parameters used in training the ANN which are the maximum and minimum values of the nine parameters given in Table 1. For input values outside the domain of boundary values, the accuracy of the predicted concrete strength cannot be confidently assured.

8. Parametric studies and sensitivity analysis:

Since the proposed ANN model was capable of predicting results that agree well with the experimental data, a parametric study was conducted to investigate the influence of the selected parameters on the compressive strength of UHPC. Plots were generated, where some of the independent parameters were held constant while the others were varied according to their practical range of values. The final ANN model is appended to this paper (see Supplementary material 1) where the model can be loaded into the MATLAB environment to carry out the parametric study. A sample of the parametric study can be found in Supplementary Material 2. It is worth mentioning that the material constituents should be normalized against cement, as explained in section Design of ANN, before executing the parametric study.

8.1.Design of the Parametric Study

Prior to performing the parametric study, the trend and distribution of data were analyzed such that practical ranges were imposed within the upper and lower boundaries of the input parameters within the ANN. Additional information regarding these statistical measurements is found in Table 1. During data collection, each experiment (row) within the data demonstrated an underlying relationship in terms of its corresponding material constituents. For instance, the increase in cement was accompanied by an increase in fly ash, silica fume and water; meaning, there existed a certain ratio between these material constituents. Therefore, when designing the matrix for parametric study the material constituents that were maintained had their ratios fixed throughout each parametric study. Table 5 summarizes the parametric study conducted in this investigation where some ratios were fixed while the remaining parameters were varied during each study.

Table 5: Summary of Parametric Study

Parametric Study	Constant ratios	Varying Parameters (kg/m^3)
Effect of fly ash at selected quantities of silica fume	water/cement ratio = 12.5%	Fly ash (0–200) Silica fume (20, 40, 60, 80)
Effect of silica fume at selected quantities of fly ash	water/cement ratio = 12.5%	Silica fume (0–200) Fly ash (40, 80, 120, 160)
Effect of water at selected quantities of fly ash	cement/silica fume ratio = 25%	water (100–350) Fly ash (40, 80, 120, 160)
Effect of water at selected quantities of silica fume	cement/fly ash ratio = 25%	water (100–350) Silica fume (20, 40, 60, 80)

8.2. Effect of fly ash at varying quantities of silica fume

Fig. 13 shows the effect of fly ash on the compressive strength of UHPC at selected quantities of silica fume (20, 40, 60, 80 kg/m^3) and at constant water/cement ratio of 12.5%. It was observed from **Fig. 13**(a) and (b) that each individual curve demonstrated an inverse relationship between the compressive strength (response variable) and the fly ash (independent variable), for all quantities of silica fume. Moreover, both mixes shown in **Fig. 13**(a) and (b) exhibited maximum compressive strength values when the quantities of fly ash and silica fume were maintained at values of 0 kg/m^3 and 20 kg/m^3, respectively. This behavior took place despite the large difference in the quantities of cement. The curve, then, experienced a slightly linear reduction in compressive strength with the continuous addition of; hence, the presence of both fly ash and silica fume weakened the mechanical performance of UHPC. However, an increase in the compressive strength was observed when the quantities of cement and water were increased by 50% without change in water cement ratio. For example, when silica fume ranges between 20 kg/m^3 and 80 kg/m^3, the UHPC mix exhibited a large reduction in compressive strength from 235.8 MPa to 155.6 MPa, at 0 kg/m^3 of fly ash as depicted in **Fig. 13**(a). On the other hand, when similar additions of silica fume were made, the mix showed less reduction in compressive strength, i.e., from 236.1 to 210.4 MPa, at 0 kg/m^3 of fly ash as shown in **Fig. 13**(b). Therefore, the increase of the quantities of cement and water of a UHPC mix tends to suppress the tendencies of reduction of UHPC's compressive strength due to increase in fly ash and silica fume. Furthermore, a substantial change in the behavior of both curves is observed when silica fume was increased – a downward concave curve, at a silica fume of 20 kg/m^3, and an upward concave curve, at a silica fume of 80 kg/m^3 are observed as shown in **Fig. 13**(a). However, when the quantities of cement and water were increase to 1200 kg/m^3 and 150 kg/m^3, all curves are downward concave curves

despite the changes in silica fume from 20 kg/m^3 to 80 kg/m^3, as shown in **Fig. 13**(b). This indicated that the presence of silica fume at high quantities of cement and water provide downward concave profile (**Fig. 13**(b)), which allows the UHPC to utilize more compressive strength compared to the mix with low quantities of cement and water, shown in **Fig. 13**(a). In summary, the following observations can be made: (a) The compressive strength of UHPC decreases with the increase in fly ash; (b) maximum compressive strength is achieved at 0 kg/m^3 of fly ash; (c) reduction in compressive strength shifts within the inverse profiles due to the addition of both cement and water; (d) lower tendencies of developing inflection points was apparent when increasing the amount of cement and water, despite extreme changes in the quantities of silica fume. **Fig. 13**(c) and (d) show surface plots of the aforementioned 2D plots in generalized contour plots.

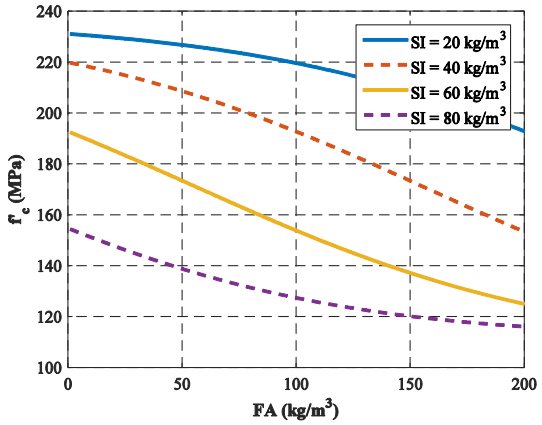

(a) Cement = 800 kg/m^3, Water = 100 kg/m^3

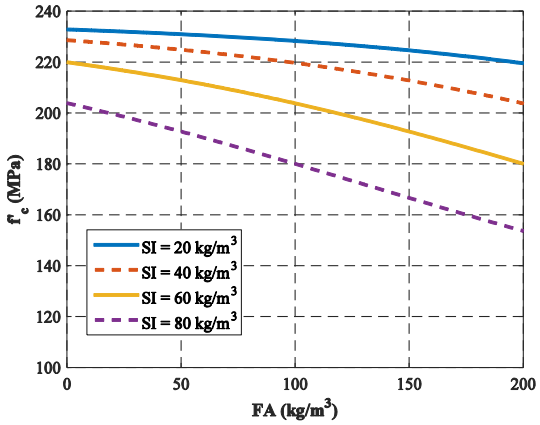

(b) Cement = 1200 kg/m^3, Water = 150 kg/m^3

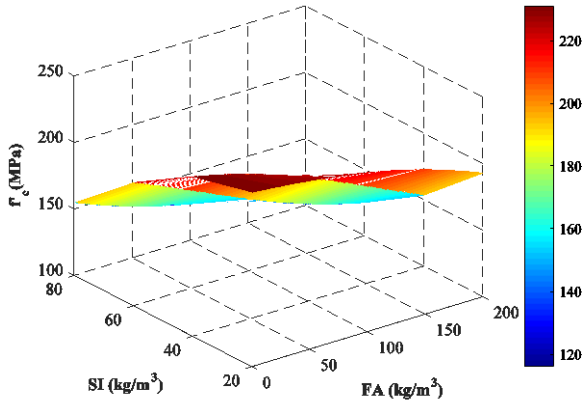

(c) Cement = 800 kg/m^3, Water = 100 kg/m^3

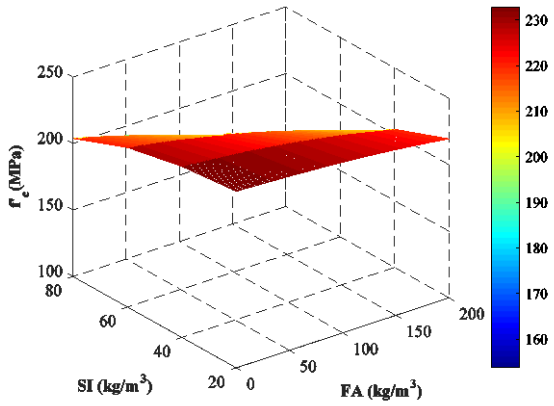

(d) Cement = 1200 kg/m^3, Water = 150 kg/m^3

Fig. 13. Effect of fly ash at varying quantities of silica fume

8.3. Effect of silica fume at varying quantities of fly ash

Fig. 14 shows the effect of silica fume on the compressive strength of UHPC at selected quantities of fly ash (40, 80, 120, 160 kg/m^3) and at constant water/cement ratio of 12.5%. Two type of relationships observed in **Fig. 14**. **Fig. 14**(a) showed a parabolic decrease in compressive strength until a local minimum value is reached and a sudden increase in compressive strength were observed with the addition of silica fume. Whereas **Fig. 14**(b) demonstrated an inverse parabolic profile until a local minimum value is reached, followed by a slight increase in the compressive strength with the addition of silica fume. An underlying difference in characteristics, in terms of both the slope and horizontal shift, is clearly shown when observing both figures. For example, in **Fig. 14**(a), the addition of fly ash (40 kg/m^3 to 160 kg/m^3) to the mix achieved maximum compressive strength values that ranged from 234.4 MPa to 225.1 MPa at 0 kg/m^3 silica fume, whereas the mix in **Fig. 14**(b) demonstrated a lesser variation in compressive strength, 236.3 MPa to 234.2 MPa, despite similar additions in the quantities of fly ash. It is clear that the increase in silica fume resulted in a decrease in the compressive strength of the UHPC until a local minimum value is reached and then its effect is reversed to an increase in compressive strength as shown in **Fig. 14**(a) and (b). This phenomenon was accompanied with a horizontal shift of the minimum values of the compressive strength, however, the addition of cement and water did not significantly impact the magnitude of the minimum compressive strength. Nevertheless, the increase in water and cement resulted in reduction in slope with the increase of silica fume as shown in **Fig. 14**(b). This indicated that such mix can sustain more strength than a mix similar to that shown in **Fig. 14**(a) in which a sudden drop is observed in the compressive strength with the addition of silica fume. This reduction in slope also impacted the scale of the amount of silica fume necessary to approximately arrive at similar minimum compressive. In summary, the following observations can be made: (a) the compressive strength of UHPC shows a semi-inverse parabolic curves and decreases with the increase in silica fume to reach distinctive local minimum; (b) maximum compressive strength is achieved at 0 kg/m^3 despite the 50% increase in cement and water; (c) at certain values of silica fume the compressive strength is not influenced by the amount of fly ash; (d) the addition of fly ash caused the minimum compressive values to exhibit horizontal shifts; (e) the increase in cement and water affected the slope of the profiles in which the compressive strength values did not vary significantly with the addition of fly ash. **Fig. 14**(c) and (d) show surface plots of the aforementioned 2D plots in generalized contour plots of the aforementioned 2D plots in generalized contour plots.

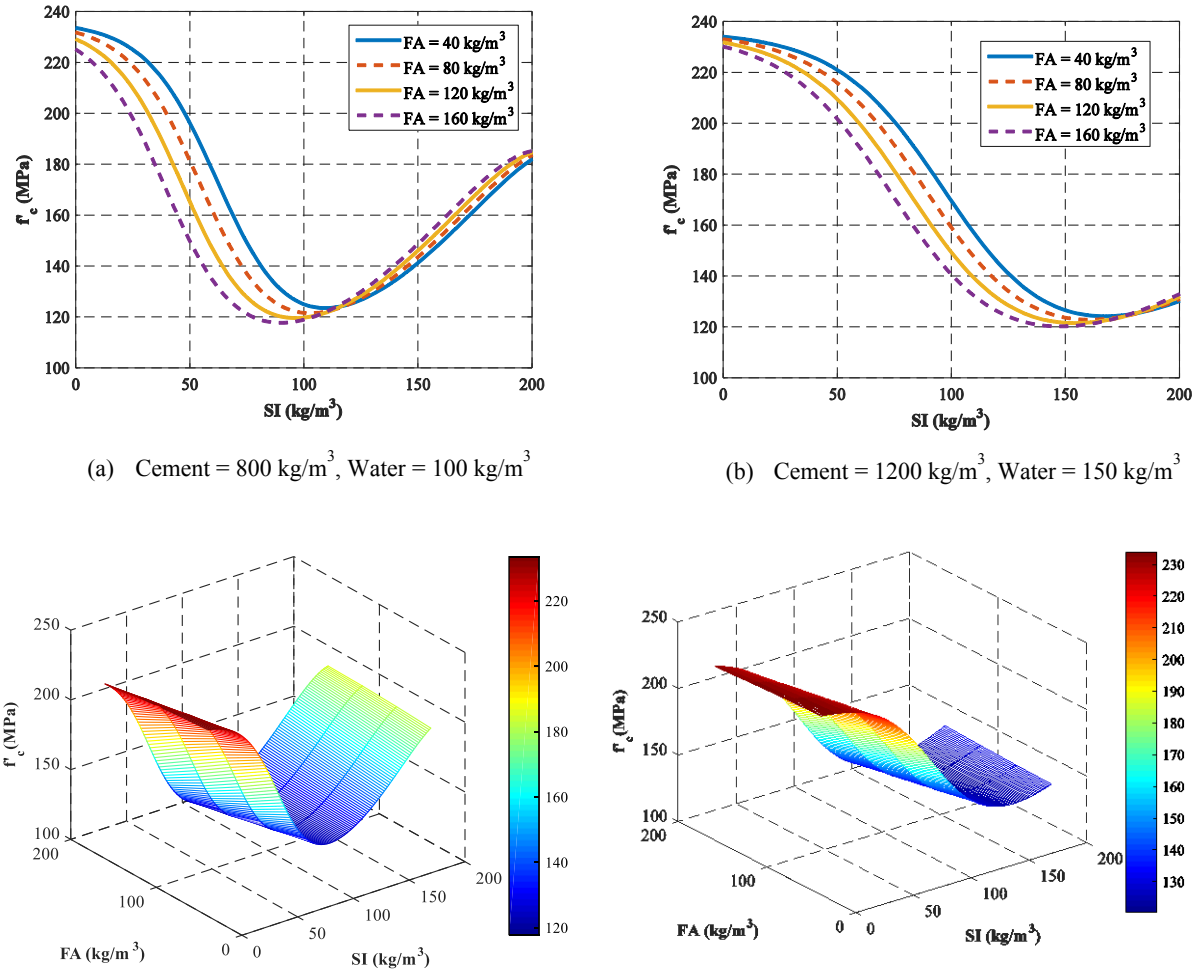

(a) Cement = 800 kg/m^3, Water = 100 kg/m^3

(b) Cement = 1200 kg/m^3, Water = 150 kg/m^3

(c) Cement = 800 kg/m^3, Water = 100 kg/m^3

(d) Cement = 1200 kg/m^3, Water = 150 kg/m^3

Fig. 14. Effect of silica fume at varying quantities of fly ash

8.4. Effect of water at varying quantities of fly ash

Fig. 15 shows the effect of water on the compressive strength of UHPC at selected quantities of fly ash (40, 80, 120, 160 kg/m^3) and at constant silica fume/cement ratio of 25%. The curves in both **Fig. 15**(a) and (b) demonstrated a positive parabolic relationship between the compressive strength and water. It is observed that both figures demonstrated relatively a small variation in compressive strength throughout the increase in the quantities of water. **Fig. 15**(a) displayed curves with a maximum and a minimum whereas the maximum compressive strength ranged between 183-186 MPa that took place at 125 kg/m^3 of water and a minimum compressive strength ranged between 135-138.4 MPa that took place at 263.3 kg/m^3 of water. The effect of fly ash on compressive strength becomes more apparent as water quantity exceeds the threshold correspond to the minimum values. On the other hand, **Fig. 15**(b) exhibited curves with a maximum compressive strength ranged between 183 - 186 MPa that was reached at 175 kg/m^3 of water. As shown in **Fig. 15**(a), the effect of fly ash on the compressive strength is slightly effective between 100 kg/m^3 and 150 kg/m^3 of water, but becomes negligible from 160 kg/m^3 to 270 kg/m^3 of water

followed by a more noticeable effect after 300 kg/m^3 of water. Similarly, increasing the cement and silica fume by 50% did not affect the maximum compressive strength, however, it shifted its location. Furthermore, the mix curves shown in **Fig. 15**(b) required additional quantities of water to reach the same maximum compressive strength as that of **Fig. 15**(a). In summary, the following observations can be made: (a) Fly ash has minimum effect on the compressive strength for large range of water quantities; (b) For low quantities of cement and silica fume, fly ash has more influence on the compressive strength at large quantities of water; (c) The maximum compressive strength is not affected by the increase in the quantity of cement and silica fume. **Fig. 15**(c) and (d) show surface plots of the aforementioned 2D plots in generalized contour plots.

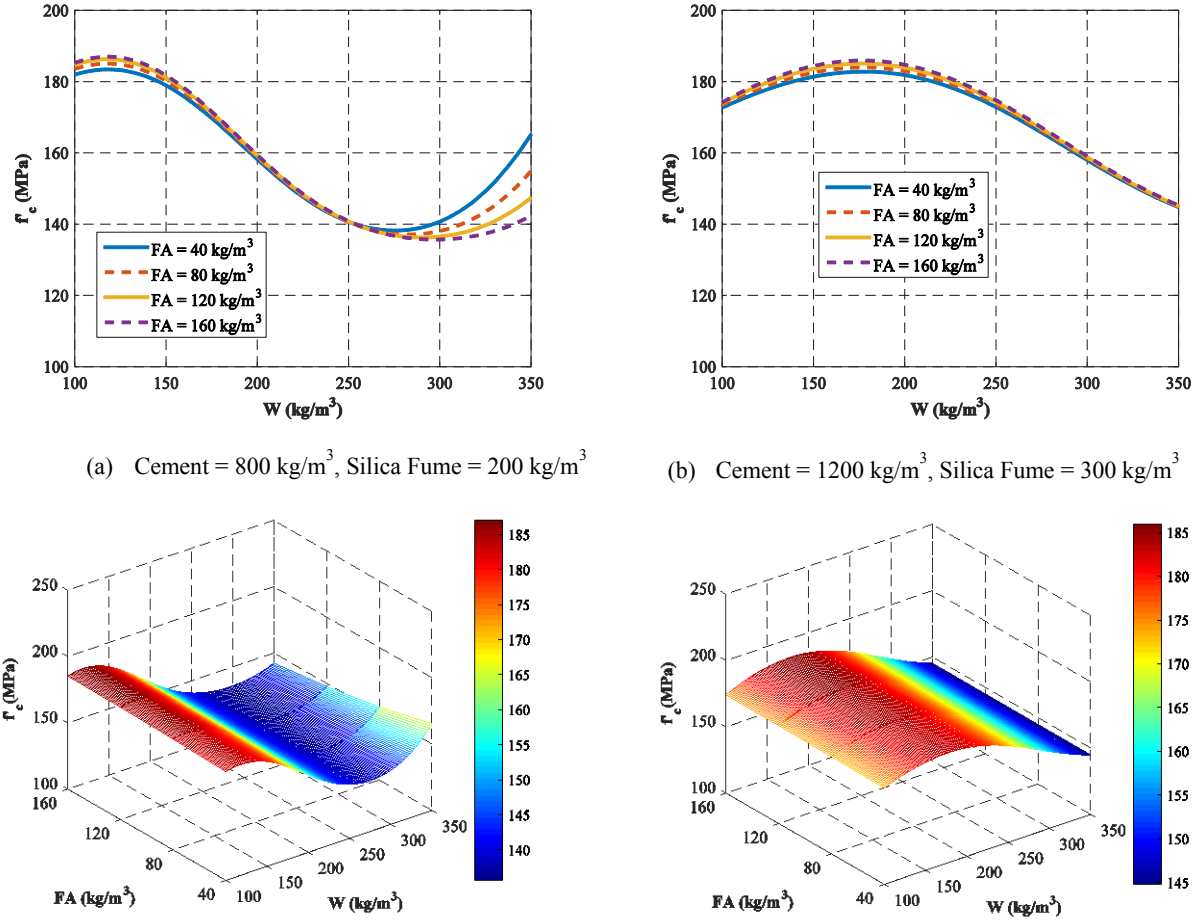

(a) Cement = 800 kg/m^3, Silica Fume = 200 kg/m^3

(b) Cement = 1200 kg/m^3, Silica Fume = 300 kg/m^3

(c) Cement = 800 kg/m^3, Silica Fume = 200 kg/m^3

(d) Cement = 1200 kg/m^3, Silica Fume = 300 kg/m^3

Fig. 15. Effect of water at varying quantities of fly ash

7.5 Effect of water at varying quantities of silica fume

Fig. 16 shows the effect of water on the compressive strength of UHPC at selected quantities of silica fume (20, 40, 60, 80 kg/m^3) and at constant fly ash/cement ratio of 25%. As shown in **Fig. 16**(a), for a given quantity of silica fume, the compressive strength of UHPC increases with the increase in water quantity until a certain compressive strength. This compressive strength shows

clear decays as silica fume increases from 20–60 kg/m^3. However, when silica fume continues to increase, the model exhibits a plateau in compressive strength wherein additional amounts of water is required to facilitate a significant increase in compressive strength. For instance, the mix with the smallest quantity of silica fume (40 kg/m^3) has the maximum compressive strength of 224 MPa reached at water quantity of 175 kg/m^3 while the mix with largest silica fume (160 kg/m^3) has the minimum compressive strength of 176 MPa reached at water quantity of 200 kg/m^3 as shown in **Fig. 16**(a). At around 200 kg/m^3 of water, all mixes with different silica fume quantities, converged to the same compressive strength of around 176 MPa after which the behavior reversed, i.e., mixes with large quantities of silica fume exhibited larger compressive strength with continuous rise with increase in water quantity. **Fig. 16**(b) shows similar behavior to that of **Fig. 16**(a), however, additional quantities of water were needed for the mixes to reach their maximum compressive strength. Similarly, all mixes shown in **Fig. 16**(b) converged at the same compressive strength of 172 MPa, however, at a larger quantity of water 340 kg/m^3 compared to the mixes of **Fig. 16**(a). In summary, the following observations can be made: (a) The curves exhibited negative vertical shifts in compressive strength similar to the inverse relationship shown in **Fig. 14**(a) and (b). (b) The curves showed horizontal shifts in the quantities of silica fume due to the sequential addition of fly ash; (c) The curves of different silica fume quantities showed different maximum compressive strength values at different quantities of water; (d) Curves with large quantities of silica fume required more water quantities to reach their maximum compressive strength. **Fig. 16**(c) and (d) show surface plots of the aforementioned 2D plots in generalized contour plots.

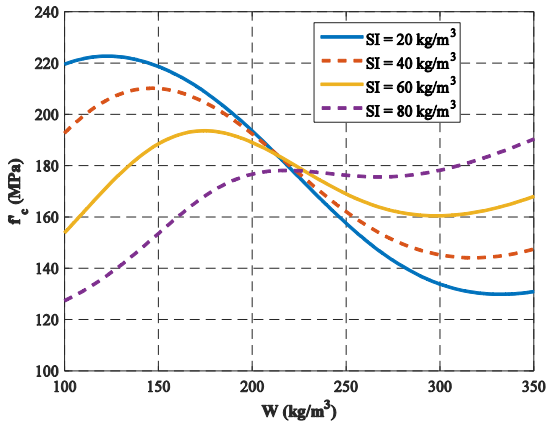

a) Cement = 800 kg/m^3, Fly ash = 200 kg/m^3

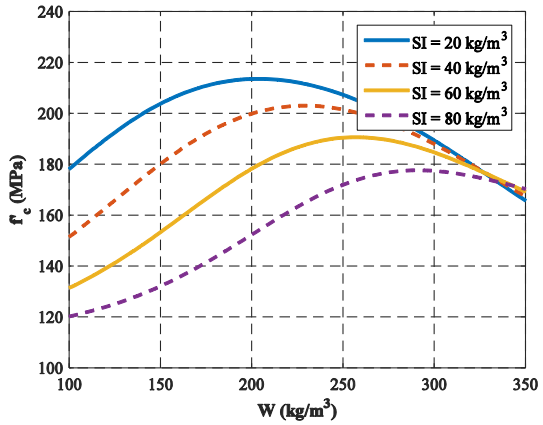

b) Cement = 1200 kg/m^3, Fly ash = 300 kg/m^3

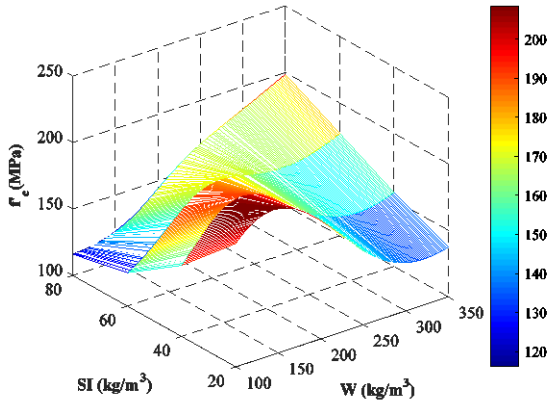

c) Cement = 800 kg/m^3, Fly ash = 200 kg/m^3

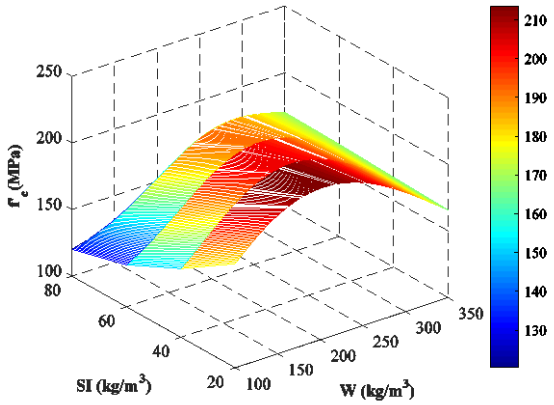

d) Cement = 1200 kg/m^3, Fly ash = 300 kg/m^3

Fig. 16. Effect of water at varying quantities of silica fume

9. Summary and conclusion

This investigation was conducted to predict the compressive strength of UHPC using ANN with the most influential parameters of the concrete mix. The investigation consisted of four major steps: (1) employment of the SFS and NID machine learning tools for identifying and selecting the most influential features or parameters; (2) analysis of selected features using BPNN; (3) modification and calibration of Abram's classical model using nonlinear regression; and (4) conduction of a sensitivity analysis to study the effect of each selected feature in the properties and behavior of UHPC. The outcomes of this study are:

- The incorporation of BPNN with SFS and NID was capable of rapidly reducing the dimensionality of the database; making it simpler for the prediction model to evaluate compressive strength values.
- The BPNN model with the four selected features predicted the results more accurately (r^2 = 80.1%; NMSE = 0.012) than the model which all eight parameters (r^2 = 21.5%;

NMSE = 0.035). Furthermore 80.1% of the values predicted using the four selected parameters are within ±15% deviation boundary limit compared to only 61% of values predicted using all eight parameters.

- Abram's classical model was modified using nonlinear regression and a final model was proposed. It yielded results that closely agreed with that of the experimental results with r^2 = 71.6% and the NMSE = 0.0645.
- It is observed that the maximum compressive strength of UHPC was achieved without the presence of silica fume, and the minimum compressive strength was achieved with additional silica fume until a specific amount of silica fume was reached.
- It was also observed that, the increase of fly ash showed a decrease in the compressive strength of UHPC. This decrease was accompanied with a horizontal shift; indicating sustainable compressive strength throughout the addition of silica fume.
- A parabolic relationship was reported when the compressive strength was plotted against the water content. Essentially, at a typical amount of fly ash and increasing quantities of silica fume, the mix requires additional water to facilitate a significant increase in compressive strength. This relationship shifts to the right when quantities of fly ash are increased, indicating larger demands of water for the additional binders (fly ash and silica fume).
- The curves developed in this study can be utilized to predict the compressive strength of UHPC mixes and to understand the underlying relationships between the compressive strength of UHPC and design mix material constituents.
- In spite of the accuracy of the ANN model developed in this investigation, it is important to emphasize that there are limitations to this accuracy. Such limitations are greatly influenced by whether the input parameters are within the domain of the applicable boundary values used in training the ANN model.

Appendix A

Table A.1: Collected database.

No.	Cement (kg/m3)	Silicafume (kg/m3)	Flyash (kg/m3)	Sand (kg/m3)	SteelFiber (kg/m3)	QuartzPowder (kg/m3)	Water (kg/m3)	Admixture (kg/m3)	fc MPa
1	750	115	125	1104	0	0	180	25	125
2	712	115	125	1142	0	0	180	25	125
3	675	115	125	1179	0	0	180	25	118
4	637	115	125	1217	0	0	180	25	118
5	750	115	125	1104	0	0	180	25	128
6	750	115	125	1103	0	0	180	25	124
7	750	115	125	1111	0	0	180	25	116
8	675	115	125	1178	0	0	180	25	128
9	637	115	125	1224	0	0	180	25	110
10	807	225	0	972	0	243	196	13	204
11	712	231	0	1020	156	211	109	30.7	138
12	778	194	189	1166	0	0	185.61	28	185
13	753	188	183	1129	0	0	170.88	27	166
14	745	186	181	1118	0	0	178.94	27	162
15	740	185	180	1110	0	0	173.19	27	200

16	778	194	189	1167	0	0	171.35	28	181
17	758	190	184	1138	0	0	170.2	28	155
18	745	186	181	1118	0	0	178.94	27	159
19	1365	151.6	0	647	0	0	151.6	30.26	136.4
20	1365	149	0	647	51.7652	0	149	30.26	137.9
21	1365	273	0	647	103.5304	0	273	30.26	140.8
22	1365	273	0	647	155.2956	0	273	30.26	155.3
23	1600	273	0	310	0	0	273	38.22	135
24	1600	273	0	310	51.7844	0	273	38.22	135.9
25	1600	320	0	310	103.6088	0	320	38.22	143.2
26	1600	320	0	310	155.4732	0	320	38.22	145.7
27	1600	320	0	310	0	0	320	77.22	124.1
28	1600	320	0	310	52.5444	0	320	77.22	128.3
29	1600	320	0	310	105.0888	0	320	77.22	127.6
30	1600	320	0	310	157.6332	0	320	78.22	144.1
31	1600	320	0	292	0	0	320	35.37	135.5
32	1600	320	0	292	51.3474	0	320	36.37	146.8
33	1600	320	0	292	102.6948	0	320	37.37	144.7
34	1600	320	0	292	154.0422	0	320	38.37	162.4
35	820	273	0	702	157	0	219	65	108
36	820	273	0	624	157	0	219	65	95
37	1040	310	0	800	0	0	240	46.944	140
38	1040	310	0	800	0	0	240	46.944	165
39	1040	310	0	800	47.8	0	240	46.944	195
40	1040	310	0	800	47.8	0	240	46.944	230
41	1040	310	0	800	0	0	240	46.944	140
42	1040	310	0	800	47.8	0	240	46.944	165
43	1040	310	0	800	47.8	0	240	46.944	210
44	510	65	0	1700	0	0	140	46.944	175
45	510	65	0	1700	11.95	0	140	46.944	195
46	510	65	0	1700	11.95	0	140	46.944	240
47	450	50	0	1720	11.95	0	140	46.944	145
48	450	50	0	1720	11.95	0	140	46.944	175
49	710	230	0	1020	156	210	110	30	119
50	967	251	0	675	430	0	244	35	128
51	711	85.32	0	0	0	0	137.2	10.665	115
52	1115	367.95	0	0	0	0	334.5	88.085	210
53	833	199.92	0	0	0	0	195.755	33.32	162
54	550	82.5	0	0	0	0	137	16.5	142
55	1107	343.17	0	0	0	0	195	61.992	217
56	715	157.3	0	0	0	0	167	30.745	178
57	800	150	0	0	20	750	230	25	119
58	1327.8	332	0	0	0	332	254.4	47.8	171

59	1050	275	0	0	470	730	190	35	175
60	657	119	0	1051	157	418	185	185	150.56
61	657	119	0	1051	0	418	185	185	121.32
62	813	203.3	0	1157	0	203.3	160.1	29.3	204
63	775	194	0	1220	0	0	165	10	170
64	845	76.1	0	0	12.6	0	175.45	0	188
65	815	65.2	0	0	8.15	0	163	0	194
66	446	32.6	0	1838	0	0	126	7.4	162
67	443	0	448	1717	0	0	228	0.4	171
68	450	0	0	1800	0	0	126	14	175
69	432	29.7	132	1636	0	0	160.2	7.9	178
70	408	39	0	1520	0	0	190	5.6	178
71	406	40.6	0	1558	0	0	185	4.3	180
72	900	135	0	1293.6	0	0	252	0	185
73	383	67.5	0	1800	0	0	125	14	187
74	775	116.3	0	1297	0	0	209.3	0	192
75	900	135	0	1189	0	0	252	0	195
76	412	41	0	1898	0	0	127	13	198
77	550	0	0	1603	0	0	151	21	199
78	398	0	185	1734.6	0	0	145	7.3	100
79	712	231	0	1231	0	0	109	30.7	101
80	786	256	0	1353	0	0	190	33	103
81	664	142	142	1231	0	0	144	56	104
82	784	256	0	1353	0	0	190	36	110
83	420	60	120	1650	0	0	138	9	110
84	786	256	0	1356	57.3	0	227	33	112
85	900	157.5	0	1030	0	0	207	0	114
86	900	157.5	0	1029.3	1.84	0	216	0	115
87	900	157.5	0	1028	2.76	0	216	0	116
88	731	239	0	1353	0	0	190	31	120
89	784	256	0	1253	0	0	190	33	123
90	800	261	0	1381	60.7	0	247	34	124
91	900	157.5	0	1017.7	11.9	0	216	0	130
92	712	231	0	1231	46.4	0	113.2	32	132
93	784	256	0	1353	0	0	190	33	134
94	800	261	0	1381	60.7	0	247	34	138
95	710	230	0	1231	47.9	0	150	13.4	138
96	1040	310	0	800	0	0	240	20.8	140
97	917	229.2	0	1443	55.8	0	202	0	145
98	784	256	0	1353	57	0	190	33	149
99	1033	258	0	1136.7	0	0	155	16.5	150
100	917	229.2	0	1443	111.6	0	202	0	153
101	786	256	0	1356	58.2	0	227	33	154

102	790	198	192	1141	37.4	0	141	28.4	155
103	665	200	0	1019	0	285	178	25	155
104	609	183	0	1334	0	263	163	21	155
105	900	220	0	1005	46.7	0	162	40	160
106	1040	310	0	800	48.2	0	240	20.8	165
107	917	229	0	1443	167.5	0	202	0	165
108	1050	275	0	730	137.5	0	190	35	169
109	775	194	0	1220	23.6	0	165	10	178
110	959	239.8	0	1055	52.3	0	163	15	200

Supplementary Material 1

Code to use ANN model:

```
load('nn_UHPC_8_3.mat')     % Load final ANN model into MATLAB   environment
fc_UHPC = net_UHPC_8_3(x); % 'fc_UHPC' is the predicted compressive
                           % strength of UHPC and 'x' is the material
                           % constituents. Size of 'fc_UHPC' and 'x' is 1 x n
                           % and m x n, where n is the number of
                           % observations (110) and m is the number of
                           % parameters ranked from C, SI, FA, and W.
```

Supplementary Material 2

Code for Effect of fly ash at varying quantities of silica fume 2-D plot.

```
clear;clc;

load('nn_UHPC_8_3.mat')          % Load ANN model.
const = 100;                     % Quantity kept constant.
C = 800;                         % Quantity of C.
W = const/C;                     % W normalized against C.

FA = linspace(0,200,150)./C;     % Variation of FA normalized against C.
xplot = linspace(0,200,150);     % Values to be viewed on
                                 % x-axis.

figure1 = figure;                % Open plot.
axes1 = axes('Parent',figure1...
    ,'YGrid','on',...
    'XGrid','on','GridAlpha',1,...
    'GridLineStyle','--',...
    'FontSmoothing','off',...
    'FontSize',12,...
    'FontName','Times');
box(axes1,'on');
hold(axes1,'on');

x_param = ones(150,4);           % Create Parametric Variable Array, where the
x_param(:,3) = FA;               % first, second, third, and four columns
x_param(:,4) = W;                % contain C, SI, FA, and W, respectively.
count = 1;
for delta = 20:20:80             % Plot line for every mix, i.e., SI ranging
    SI = delta/C;                % from 20-80 kg/m^3, normalized against C.
    x_param(:,2) = SI;
    pred(count).plot = ...       % Calculate predictions.
        net_UHPC_8_3(x_param');

    plot1(count) = plot(xplot,...
        pred(count).plot,'LineWidth',2);

    hold on
    count = count + 1;
end
```

```
set(plot1(1),'DisplayName'...    % Change name of plots for labels in
    ,'SI = 20 kg/m^3',...        % legend.
    'MarkerSize',1);
set(plot1(2),'DisplayName'...
    ,'SI = 40 kg/m^3',...
    'LineStyle','--');
set(plot1(3),'DisplayName'...
    ,'SI = 60 kg/m^3');
set(plot1(4),'DisplayName'...
    ,'SI = 80 kg/m^3'...
    ,'LineStyle','--');


xlabel('FA (kg/m^3)',...         % Create x and y labels.
    'FontWeight','bold');
ylim([100,240])
ylabel('f''_c (MPa)',...
    'FontWeight','bold');
legend1 = legend(axes1,'show');
set(legend1,'FontSize',12);
```

Code for Effect of fly ash at varying quantities of silica fume 3-D plot.

```
clear;clc;

load('nn_UHPC_8_3.mat')          % Load ANN model.
const = 100;                     % Quantity kept constant.
C = 800;                         % Quantity of C.
W = const/C;                     % W normalized against C.

FA = linspace(0,200,150)./C;     % Variation of FA normalized against C.
xplot = linspace(0,200,150);     % Values to be viewed on
                                 % x-axis.

figure1 = figure;                % Open plot.
colormap('jet');
axes1 = axes('Parent',...
    figure1,'GridAlpha',1,...
    'GridLineStyle','--',...
    'FontSize',12,...
    'FontName','Times');
view(axes1,[-37.5 30]);
grid(axes1,'on');
hold(axes1,'on');

x_param = ones(150,4);           % Create Parametric Variable Array, where the
x_param(:,3) = FA;               % first, second, third, and four columns
x_param(:,4) = W;                % contain C, SI, FA, and W, respectively.
count = 1;

for delta = 20:20:80             % Plot line for every mix, i.e., SI ranging
    SI = delta/C;                % from 20-80 kg/m^3, normalized against C.
```

```
    x_param(:,2) = SI;
    pred(count,1:150,1) = ...    % Calculate predictions.
         net_UHPC_8_3(x_param');

    y3d(count) = delta;

    count = count + 1;
end

x3d = xplot;                     % Mesh 3D contour plot.
z3d = pred;

mesh(x3d,y3d,z3d)

xlabel('FA (kg/m^3)',...         % Create x, y, and z labels.
    'FontWeight','bold',...
    'FontSize',12);
xlim([0,200])
ylabel('SI (kg/m^3)'...
    ,'FontWeight','bold',...
    'FontSize',12);
zlabel('f''_c(MPa)',...
    'FontWeight','bold',...
    'FontSize',12);
zlim([100,250])

colorbar('peer',...              % Create color bar.
    axes1,'Color',[0 0 0]);
```

Reference:

[1] S. Haykin, Neural Networks and Learning Machines, third ed., Pearson Education, Inc., Upper Saddle River, New Jersey 07458, USA, 2009, pp. 1–936.

[2] I. Flood, Neural networks in civil engineering: a review, Civil and structural engineering computing (2001), Saxe-Coburg Publications, 2001, pp. 185–209.

[3] M. A. Shahin, M. B. Jaksa, H. R. Maier, State of the art of artificial neural networks in geotechnical engineering. Electronic J Geotech Eng (2008). http://www.ejge.com.

[4] J. A. Abdalla, M. F. Attom, R Hawileh, Artificial neural network prediction of factor of safety of slope stability of soils, in: The 14th International Conference on Computing in Civil and Building Engineering, Moscow, Russia, 2012.

[5] S. K. Das, Artificial Neural Networks in Geotechnical Engineering: Modeling and Application Issues. Metaheuristics in Water, Geotechnical and Transport Engineering (2013) 231–270.

[6] J. A. Abdalla, M. F. Attom, R Hawileh, Prediction of minimum factor of safety against slope failure in clayey soils using artificial neural network, Environmental Earth Sciences. 73 (2015) 5463-5477. https://doi.org/10.1007/s12665-014-3800-x.

[7] P. Srisuksomwong & J. Pekkoh (2020). Artificial Neural Network Model to Prediction of

Eutrophication and Microcystis Aeruginosa Bloom. Emerging Science Journal, Vol. 4, No. 2, April, (2020) 129-135.

[8] Z. Waszczyszyn and L. Ziemianski, Neural networks in mechanics of structures and materials – new results and prospects of applications, Computers and Structures. 79 (2001) 2261–2276. https://doi.org/10.1016/S0045-7949(01)00083-9.

[9] M. Hadi, Neural networks applications in concrete structures, Computers and structures. 81 (2003) 373-381. https://doi.org/10.1016/S0045-7949(02)00451-0.

[10] A. W. C. Oreta, Simulating size effect on shear strength of RC beams without stirrups using neural networks, Eng. Struct. 26 (2004) 681–691. https://doi.org/10.1016/j.engstruct.2004.01.009.

[11] B. B. Adhikary and H. Mutsuyoshi, Prediction of shear strength of steel fiber RC beams using neural networks, Constr. Build. Mater. 20 (2006) 801–811. https://doi.org/10.1016/j.conbuildmat.2005.01.047.

[12] J. A. Abdalla, A. Elsanosi and A. Abdelwahab, Modeling and simulation of shear resistance of R/C beams using artificial neural network, Journal of the Franklin Institute. 344 (2007) 741-756. https://doi.org/10.1016/j.jfranklin.2005.12.005.

[13] J. A. Abdalla, R. Hawileh and A. Al-Tamimi, Prediction of FRP-concrete ultimate bond strength using Artificial Neural Network, The 4th International Conference on Modeling, Simulation and Applied Optimization (ICMSAO), Zallaq, Bahrain, 2011.

[14] H. M. Tanarslan, M. Secer, and A. Kumanlioglu, An approach for estimating the capacity of RC beams strengthened in shear with FRP reinforcements using artificial neural networks, Constr. Build. Mater. 30 (2012) 556–568. https://doi.org/10.1016/j.conbuildmat.2011.12.008.

[15] J. A. Abdalla, E. I. Saqan and R. A. Hawileh, Optimum seismic design of unbonded post-tensioned precast concrete walls using ANN, Computers and Concrete. 13 (2014) 547-567. https://dx.doi.org/10.12989/cac.2014.13.4.547.

[16] J. A. Abdalla and R. A. Hawileh, Energy-based predictions of number of reversals to fatigue failure of steel bars using artificial neural network, in: The 13th International Conference on Computing in Civil and Building Engineering, Sharjah, UAE, 2010.

[17] J. A. Abdalla and R. Hawileh, Modeling and simulation of low-cycle fatigue life of steel reinforcing bars using artificial neural network, Journal of the Franklin Institute. 3481 (2011) 393-1403. https://doi.org/10.1016/j.jfranklin.2010.04.005.

[18] J. C. F. Pujol and J. M. A. Pinto, A neural network approach to fatigue life prediction, International Journal of Fatigue. 33 (2011) 313-322. https://doi.org/10.1016/j.ijfatigue.2010.09.003.

[19] J. A. Abdalla and R. A. Hawileh, Artificial neural network predictions of fatigue life of steel bars based on hysteretic energy, Journal of Computing in Civil Engineering. 27 (2013) 489-496. https://doi.org/10.1061/(ASCE)CP.1943-5487.0000185.

[20] J.F. Durodola, S. Ramachandra, S. Gerguri, N.A. Fellows, Artificial neural network for random fatigue loading analysis including the effect of mean stress, International Journal of Fatigue. 111 (2018) 321–332. https://doi.org/10.1016/j.ijfatigue.2018.02.007.

[21] H. Naderpour, A. H. Rafiean, and P. Fakharian, Compressive strength prediction of environmentally friendly concrete using artificial neural networks, Journal of Building Engineering. 16 (2018) 213–219. https://doi.org/10.1016/j.jobe.2018.01.007.

[22] A. Heidari, M. Hashempour, and D. Tavakoli, Using of Backpropagation Neural Network in Estimating of Compressive Strength of Waste Concrete, Soft Computing in Civil Engineering. 1 (2017) 54–64. https://doi.org/10.22115/SCCE.2017.48040.

[23] J. Sobhani, M. Najimi, Numerical study on the feasibility of dynamic evolving neural-fuzzy inference system for approximation of compressive strength of dry-cast concrete, Applied Soft Computing. 24 (2014) 572–584. https://doi.org/10.1016/j.asoc.2014.08.010.

[24] F. Deng, Y. He, S. Zhou, Y. Yu, H. Cheng, and X. Wu, Compressive strength prediction of recycled concrete based on deep learning, Construction and Building Materials. 175 (2018) 562–569. https://doi.org/10.1016/j.conbuildmat.2018.04.169.

[25] E.M. Golafshani, A. Behnood, Automatic regression methods for formulation of elastic modulus of recycled aggregate concrete, Applied Soft Computing. 64 (2018) 377–400. https://doi.org/10.1016/j.asoc.2017.12.030.

[26] G. Tayfur, T. K. Erdem, and K. Önder, Strength Prediction of High-Strength Concrete by Fuzzy Logic and Artificial Neural Networks, Journal of Materials in Civil Engineering. 26 (2014) 1–7. https://doi.org/10.1061/(ASCE)MT.1943-5533.0000985.

[27] D. K. Bui, T. Nguyen, J. S. Chou, H. Nguyen-Xuan, T. D. Ngo, A modified firefly algorithm-artificial neural network expert system for predicting compressive and tensile strength of high-performance concrete, Construction and Building Materials. 180 (2018) 320-333. https://doi.org/10.1016/j.conbuildmat.2018.05.201.

[28] Y. Yu, W. Li, J. C. Li, T. N. Nguyen, A novel optimized self-learning method for compressive strength prediction of high performance concrete, Construction and Building Materials. 184 (2018) 229-247. https://doi.org/10.1016/j.conbuildmat.2018.06.219.

[29] E. Ghafari, M. Bandarabadi, H. Costa, E. Júlio, Design of UHPC using artificial neural networks, in: A.M. Brandt, J. Olek, M.A. Glinicki, C.K.Y.B.T.-B.M.C. 10 Leung (Eds.), Woodhead Publishing, 2012: pp. 61–69. doi:https://doi.org/10.1533/9780857099891.61.

[30] A. D. Janusz Kasperkiewicz, Janusz Rucz, HPC strength prediction using artificial neural network, Journal of Computing in Civil Engineering. 9 (1996) 279–284. https://doi.org/10.1061/(ASCE)0887-3801(1995)9:4(279).

[31] C. T.G Awodiji, D. O. Onwuka, C. E. Okere, and O. M. Ibearugbulem, Anticipating the Compressive Strength of Hydrated Lime Cement Concrete Using Artificial Neural Network Model, Civil Engineering Journal. 4 (2018) 3005–3018. http://dx.doi.org/10.28991/cej-03091216.

[32] C. Shi, Z. Wu, J. Xiao, D. Wang, Z. Huang, and Z. Fang, A review on ultra high performance concrete: Part I. Raw materials and mixture design, Construction and Building Materials. 101 (2015) 741–751. https://doi.org/10.1016/j.conbuildmat.2015.10.088.

[33] J. L. Y. Zhang, W. Sun, S. Liu, C. Jiao, Preparation of C200 green reactive powder concrete and its static-dynamic behaviors, Cement and Concrete Composites. 30 (2008) 831–838. https://doi.org/10.1016/j.cemconcomp.2008.06.008.

[34] Y. W. W. Zheng, B. Luo, Compressive and tensile properties of reactive powder concrete with steel fibres at elevated temperatures, Construction and Building Materials. 41 (2013) 844–851. https://doi.org/10.1016/j.conbuildmat.2012.12.066.

[35] A. A. Pishro and X. Feng. Experimental Study on Bond Stress between Ultra High Performance Concrete and Steel Reinforcement. Civil Engineering Journal. Vol. 3, No. 12, (2017) 1235-1245.

[36] K. Q. Yu, J. T. Yu, J. G. Dai, Z. D. Lu, and S. P. Shah, Development of ultra-high performance engineered cementitious composites using polyethylene (PE) fibers, Construction and Building Materials. 158 (2018) 217–227. https://doi.org/10.1016/j.conbuildmat.2017.10.040.

[37] A. A. Pishro and X. Feng. Experimental and Numerical Study of Nano-Silica Additions on the Local Bond of Ultra-High Performance Concrete and Steel Reinforcing Bar. Civil Engineering Journal. Vol. 3, No. 12, (2017) 1339-1348.

[38] K. Wille, A. E. Naman, and G. J. Parra-Montesinos, Ultra-High Performance Concrete with Compressive Strength Exceeding 150 MPa (22ksi) : A Simpler Way, ACI Materials Journal. 108 (2011) 46–53. https://doi.org/10.14359/51664215.

[39] S. Abbas, M. L. Nehdi, and M. A. Saleem, Ultra-High Performance Concrete: Mechanical Performance, Durability, Sustainability and Implementation Challenges, International Journal of Concrete Structures and Materials. 10 (2016) 271–295. https://doi.org/10.1007/s40069-016-0157-4.

[40] N. A. Soliman and A. Tagnit-Hamou, Using glass sand as an alternative for quartz sand in UHPC, Construction and Building Materials. 145 (2017) 243–252. https://doi.org/10.1016/j.conbuildmat.2017.03.187.

[41] E. Ghafari, M. Bandarabadi, H. Costa, and E. Júlio, Prediction of Fresh and Hardened State Properties of UHPC : Comparative Study of Statistical Mixture Design and an Artificial Neural Network Model, Journal of Materials in Civil Engineering. 27 (2015) 1–11. https://doi.org/10.1061/(ASCE)MT.1943-5533.0001270.

[42] N. Gu, M. Fan, L. Du, and D. Ren, Efficient sequential feature selection based on adaptive eigenspace model, Neurocomputing. 161 (2015) 199–209. https://doi.org/10.1016/j.neucom.2015.02.043.

[43] J. Cai, J. Luo, S. Wang, and S. Yang, Feature selection in machine learning: A new perspective, Neurocomputing. 300 (2018) 70–79.

https://doi.org/10.1016/j.neucom.2017.11.077.

[44] R. Kohavi and G. H. John, Wrappers for feature subset selection, Artificial Intelligence. 97 (1997) 273–324. https://doi.org/10.1016/S0004-3702(97)00043-X.

[45] H. Zhou, M. You, L. Liu, and C. Zhuang, Sequential data feature selection for human motion recognition via Markov blanket, Pattern Recognition Letters. 86 (2017) 18–25. https://doi.org/10.1016/j.patrec.2016.12.008.

[46] V. F. Rodriguez-Galiano, J. A. Luque-Espinar, M. Chica-Olmo, and M. P. Mendes, Feature selection approaches for predictive modelling of groundwater nitrate pollution: An evaluation of filters, embedded and wrapper methods, Science of The Total Environment. 624 (2018) 661–672. https://doi.org/10.1016/j.scitotenv.2017.12.152.

[47] S. L. Özesmi and U. Özesmi, An artificial neural network approach to spatial habitat modelling with interspecific interaction, Ecological Modelling. 116 (1999) 15–31. https://doi.org/10.1016/S0304-3800(98)00149-5.

[48] K. Habel, M. Viviani, E. Denarié, and E. Brühwiler, Development of the mechanical properties of an Ultra-High Performance Fiber Reinforced Concrete (UHPFRC), Cement and Concrete Research. 36 (2006) 1362–1370. https://doi.org/10.1016/j.cemconres.2006.03.009.

[49] M. Ghrici, S. Kenai, and M. Said-Mansour, Mechanical properties and durability of mortar and concrete containing natural pozzolana and limestone blended cements, Cement and Concrete Composites. 109 (2017) 542–549. https://doi.org/10.1016/j.cemconcomp.2007.04.009.

[50] B. A. Graybeal, Compressive Behavior of Ultra-High-Performance Fiber-Reinforced Concrete, ACI Materials Journal. 104 (2007) 146-152. https://doi.org/10.14359/18577.

[51] A. M. T. Hassan, S. W. Jones, and G. H. Mahmud, Experimental test methods to determine the uniaxial tensile and compressive behaviour of Ultra High Performance Fibre Reinforced Concrete(UHPFRC), Construction and Building Materials. 37 (2012) 874–882. https://doi.org/10.1016/j.conbuildmat.2012.04.030.

[52] K. Wille and C. Boisvert-Cotulio, Material efficiency in the design of ultra-high performance concrete, Construction and Building Materials. 86 (2015) 33–43. https://doi.org/10.1016/j.conbuildmat.2015.03.087.

[53] H. O. Jang, H. S. Lee, K. Cho, and J. Kim, Experimental study on shear performance of plain construction joints integrated with ultra-high performance concrete (UHPC), Construction and Building Materials. 152 (2017) 16–23. https://doi.org/10.1016/j.conbuildmat.2017.06.156.

[54] M. Hassan and K. Wille, Experimental impact analysis on ultra-high performance concrete (UHPC) for achieving stress equilibrium (SE) and constant strain rate (CSR) in Split Hopkinson pressure bar (SHPB) using pulse shaping technique, Construction and Building Materials. 144 (2017) 747–757. https://doi.org/10.1016/j.conbuildmat.2017.03.185.

[55] M. Shafieifar, M. Farzad, and A. Azizinamini, Experimental and numerical study on mechanical properties of Ultra High Performance Concrete (UHPC), Construction and Building Materials. 156 (2017) 402–411. https://doi.org/10.1016/j.conbuildmat.2017.08.170.

[56] A. Alsalman, C. N. Dang, G. S. Prinz, and W. M. Hale, Evaluation of modulus of elasticity of ultra-high performance concrete, Construction and Building Materials. 153 (2017) 918–928. https://doi.org/10.1016/j.conbuildmat.2017.07.158.

[57] R. Zhong, K. Wille, and R. Viegas, Material efficiency in the design of UHPC paste from a life cycle point of view, Construction and Building Materials. 160 (2018) 505–513. https://doi.org/10.1016/j.conbuildmat.2017.11.049.

[58] M. Alkaysi and S. El-Tawil, Factors affecting bond development between Ultra High Performance Concrete (UHPC) and steel bar reinforcement, Construction and Building Materials. 144 (2017) 412–422. https://doi.org/10.1016/j.conbuildmat.2017.03.091.

[59] M. G. Sohail et al., Advancements in Concrete Mix Designs: High-Performance and Ultrahigh-Performance Concretes from 1970 to 2016, Journal of Materials in Civil Engineering. 30 (2018) 1–20. https://doi.org/10.1061/(ASCE)MT.1943-5533.0002144.

[60] M. I. A. Lourakis and A. Argyros, The Design and Implementation of a Generic Sparse Bundle Adjustment Software Package Based on the Levenberg-Marquardt Algorithm, Technical Report 340, Institution of Computer Science-FORTH. (2004). http://www.ics.forth.gr/lourakis/sba.

[61] MATLAB 2015a, The MathWorks, Natick, Massachusetts, United States, 2015.

[62] S. Popovics, Strength and related properties of concrete: a quantitative approach, New York, NY: Wiley, 1998.

View publication stats